Composite wing box deformed-shape reconstruction based on measured strains: Optimization and comparison of existing approaches

Composite wing box deformed-shape reconstruction based on measured strains: optimization and comparison of existing approaches

Marco Esposito*, Marco Gherlone
Politecnico di Torino
Department of Mechanical and Aerospace Engineering
Corso Duca degli Abruzzi 24, 10129 Torino, Italy

Abstract

The reconstruction of the displacement field of a structure (shape sensing) has become crucial for the Structural Health Monitoring of aerospace structures and for the progress of the recently developing morphing structures. As a consequence, shape sensing techniques based on discrete surface strains measurements have seen a consistent expansion in the last few years. In this paper, the three main shape sensing methods, the Modal Method, the Ko's displacements theory and the inverse Finite Element Method, are presented. The most recent and also novel improvements are discussed and added to the methods' formulations. Then, the three methods are numerically applied to a complex aerospace structure such as that of a composite wing box experiencing bending and twisting deformations. For the first time, a detailed investigation on the optimal strain sensors configuration is performed for all the three techniques simultaneously. Finally, the methods' performances, in terms of accuracy of the reconstruction and of number of required sensors, are compared. The three methods show different characteristics that make them suitable for different applications, depending on the level of accuracy and the number of strain information required. The iFEM is proven to be the more accurate but the more demanding in terms of required sensors; the Ko's displacement theory is capable of giving a rough estimation of the displacement field, but requires a small amount of sensors; the Modal Method represents a trade-off between the other two in terms of accuracy and number of sensors required.

Keywords:
Structural Health Monitoring; Shape Sensing; Strain Measurement; Wing Box.

1 Introduction

Structural Health Monitoring may have in the future a crucial role in the design and maintenance of aerospace wing structures, where the use of composite materials is rapidly increasing. Since damage-tolerance design of composite is strongly influenced by the difficulties in detecting non-visible damages, techniques capable of monitoring damages in real time through the reconstruction of structural shape could significantly improve composite wing structures performance and service life. Moreover, the recent development of morphing structures [1] can benefit from the application of the shape sensing techniques. Thanks to the real-time evaluation of the displacement field, a feedback control system for the morphing mechanisms can be implemented [2].
The recent advancement in the strain sensing technology is also a factor that facilitated the progress in the shape sensing methods based on the discrete strain measurements. The development of fiber optic strain sensing

*Corresponding author: marco.esposito@polito.it (Marco Esposito)

systems gives the opportunity to have a multiplex, highly sensible and highly integrated sensor for strain measurement of composite structures. In fact, the Fiber Optic Systems based on fiber Bragg gratings (FBGs) and, more recently, distributed systems based on Rayleigh scattering and Optical Frequency Domain Reflectometry (OFDR), can be embedded in composite laminates during the layup phase [3, 4].

Four main categories of shape sensing methods based on discrete strain measurements have been proposed: (1) methods based on numerical integration of experimental strains [5–11]; (2) methods using global or piecewise linear continuous basis functions to approximate the displacement field [12–25]; (3) inverse Finite Element Methods (iFEM), based on a finite-element discretization and on a variational principle [26–46]; (4) method based on the use of the Artificial Neural Networks (ANNs) [47, 48].

This study will focus on the three methods that have proven to be more successful for aerospace applications in the existing literature, the Ko displacement's theory, the Modal Method and the inverse Finite Element Method. They belong to the first, the second and the third category respectively. For an extensive review of the other existing methods and their application, refer to [49].

The method proposed by Ko et al. [8] (Ko's Displacement theory) is based on the classical Bernoulli-Euler beam theory and it has been designed for the reconstruction of the deflection of wing structures. Axial strains are measured at discrete locations along the wing span and curvature can be easily evaluated. Double integration of the curvature provides the deflection shape at the same discrete locations. In addition, using more than one sensing line along the wing span, it is possible to evaluate the cross-sectional twist angle due to torsion. The method was applied to the doubly-tapered wing of the Ikhana unmanned vehicle in [9]. The test was conducted on a high-fidelity FE model of the wing and resulted in an accurate prediction of the deformed shape of the wing model. In [7], an experimental validation of the method was accomplished. The method was proven capable of evaluating the tip deflection of the Global Observer UAV's wing during a ground test. The vehicle was equipped with two strain sensing lines of optical fibers along the span. A recent improvement of the Ko's approach is due to Pak and allows the full reconstruction of the displacement field by means of a modal transformation [50]. Pak's methodology is based on a two-step process. In the first step the deflection along the sensing lines are computed using the classical Ko's displacements theory. The second step expands the shape sensing to the whole structural domain using the SEREP modal transformation [51]. Pak validated the two-step procedure numerically and experimentally on a wing shaped flat plate.

The methods based on basis functions use known spatial functions and unknown weights to describe the displacement field of the structure. The weights are determined through the fitting of the reconstructed strains function to the experimental discrete strains. In particular, the Modal Method makes use of the modal shapes as basis functions. Foss and Haugse [15] and Pisoni et al. [23] introduced the method. Foss and Haugse used experimentally measured modal characteristics to predict the static deformation of an aluminum cantilevered plate. They also performed a study on the influence of the number and position of the strain sensors on a numerically simulated plate. The possibility to use genetic algorithms to optimize the sensors configuration was also explored. Pisoni et al. applied the method to the reconstruction of the displacements of a vibrating clamped beam. The evaluation of the modal shapes of the structure is mandatory for the application of this method although it can often result in an onerous process. The previously cited works used experimentally computed modal characteristics of the structure. Differently, Bogert et al. [13] used modal characteristics computed numerically through a FE model for the application of the Modal Method to a cantilevered plate. The study also included a criterion for the selection of the modes more suitable for the application of the method. The selection criterion is based on the evaluation of the strain energy of each mode. Rapp et al. [24] examined in deep the influence of the number and location of strain sensors on the accuracy of the method. The authors highlighted the importance of the strains location when using a little number of discrete strain measurements.

The inverse Finite Element Method is based on the minimization of a weighted-least-squares functional that expresses the error between the strains due to the reconstructed displacements, discretized using finite elements, and the actually measured ones. The formulation only makes use of strain-displacements relations. Therefore, any information about materials or load acting on the structure is unnecessary. The iFEM method has been introduced by Tessler and Sprangler [44]. They developed a three-node inverse shell element, iMIN3, based on the

Mindlin plate theory. The method was extended to truss and beam structures by Gherlone et al. [30, 31]. Since its first development, the iFEM method has been successfully applied to a wide range of structural problems, both by numerical simulation and by experimental campaigns. Tessler et al. [45] numerically reconstructed the full-field structural displacements of a plate under bending loads. Quach et al. [43] demonstrated the applicability of the iMIN3 elements to the detection of structural anomaly by an experimental application of iFEM to an aluminum bar specimen. Gherlone et al. [49] validated the full-field displacements reconstruction capability of the Inverse Finite Element Method on the application to a real wing-shaped thin aluminum plate. Recently, Miller et al. [41] applied the iFEM to a half-span wing model with the aim of computing the wing deflection, the wing twist and the internal loads. They used the classical triangular inverse element formulation and compared the effect of three different sparse strains sensors configurations. They also evaluated the effect of noisy sensors data.

To further enrich the iFEM capability, the elements library was extended by the implementation of a four-node quadrilateral element by Kefal et al. [32], the iQS4. The iQS4 was developed using the Mindlin plate theory and it has 6 degrees of freedom per node, including hierarchical drilling rotations. The new element was tested on a cantilevered plate subjected to a bending load and a cantilevered beam under transverse shear loading. The iQS4 was subsequently applied by Kefal et al. to the study of marine structures. The reconstruction of the displacements and the stresses of a typical chemical tanker mid-ship [33], of a Panamax container ship [34] and of a capsize bulk carrier [37] were successfully accomplished by the authors. Recently, another marine application, the monitoring of cylindrical structures, inspired the development of a eight-node inverse curved element, the iQS8 [38].

Few comparative studies involving the shape sensing methods have been carried on. Devorkian et al. [52] compared the Ko's displacement theory and the Modal Method on a swept cantilevered plate. The only comparison of the three methods was performed by Gherlone et al. [49]. The three methods were applied on a real swept wing-shaped aluminum plate. In both these works a study on the effect of sensors configuration is missing.

Aim of this work is to perform a comparative study on the performances of the Ko's Displacement theory, of the Modal Method and of iFEM, for the structural shape reconstruction of a complex structure such as that of a composite wing box. The novelty of this work is represented by the structural complexity that the three methods have to address and by the implementation of the most recent improvements in the application of the Ko's Displacement theory and of the iFEM, i.e., the modal extension due to Pak's work and the 4-node element formulation due to Kefal et al. A rigorous investigation of the optimal strain sensors configuration for all the three methods is also conducted for the first time. A high-fidelity FE model of the wing box undergoing bending and torsion is used to provide both input strain data and the displacement field as reference result. The three methods are compared on the evaluation of the full vertical displacement field of the wing box.

The paper content is organized as follows. In sections 2-4 the three investigated shape sensing methods are described in detail. In section 5, the test case and the results obtained during the research campaign are presented. In this section the wing box geometry, the load configuration and the sensors optimization process are reported. In section 6, the obtained results are further discussed and some conclusions and recommendations for future research development are proposed.

2 Modal Method

The Modal Method (MM), firstly introduced by Foss and Haugse [15], is based on a modal transformation algorithm. This algorithm makes use of the modal characteristics of the structure in order to recover the displacement field from discrete stain data.

Using the classical modal transformation from structural dynamics and a FE discretization of the displacement field, both the displacements and the strains can be expressed in terms of the M modal coordinates $\boldsymbol{q}$

$$\boldsymbol{w} = \boldsymbol{\Phi}_d \, \boldsymbol{q} \tag{1}$$

$$\boldsymbol{\varepsilon} = \boldsymbol{\Phi}_s \, \boldsymbol{q} \tag{2}$$

where $\boldsymbol{w}_{Dx1}$ is the displacement degrees-of-freedom vector, $\boldsymbol{\varepsilon}_{Sx1}$ is the discrete strain vector, $[\boldsymbol{\Phi}_d]_{DxM}$ is the displacement modal shapes matrix (simply known as modal matrix) and $[\boldsymbol{\Phi}_s]_{SxM}$ is the strain modal shapes matrix. More precisely, the i-th column of the $\boldsymbol{\Phi}_s$ matrix correspond to the strain vector associated to the i-th modal shape.
Displacement modal shapes and strain modal shapes can be easily computed through a Finite Element analysis but they could be significantly difficult to estimate experimentally. The typical modal excitation source adopted during modal tests results in very low strains, therefore requiring high degrees of accuracy, which are not always easily achievable by measurement systems [15].
From Eq. 2 it is possible to express the modal coordinates in function of the strain modal shapes

$$\boldsymbol{q} = \boldsymbol{\Phi}_s^{-1} \, \boldsymbol{\varepsilon} \tag{3}$$

Then, substituting Eq. 3 into Eq. 1,

$$\boldsymbol{w} = \boldsymbol{\Phi}_d \boldsymbol{\Phi}_s^{-1} \, \boldsymbol{\varepsilon} \tag{4}$$

thus obtaining an expression of the displacements in terms of modal matrices and strain vector.
Since in practical situations it is unlikely that the number of available strains (S) is equal to the number of calculated modes (M), the method has to deal with non squared matrices. This problem is easily overcome by the use of a least-square approach by means of Moore-Penrose pseudo inverse matrix formulation. Eq. 3 is modified as follows

$$\boldsymbol{q} = (\boldsymbol{\Phi}_s^T \boldsymbol{\Phi}_s)^{-1} \boldsymbol{\Phi}_s^T \, \boldsymbol{\varepsilon} \tag{5}$$

and consequently Eq. 4 is

$$\boldsymbol{w} = \boldsymbol{\Phi}_d (\boldsymbol{\Phi}_s^T \boldsymbol{\Phi}_s)^{-1} \boldsymbol{\Phi}_s^T \, \boldsymbol{\varepsilon} \tag{6}$$

In the case of $S < M$, the problem would admit infinite solutions whereas, with $S > M$, the number of equations is higher than the number of unknowns and the problem can be solved with the aforementioned least-square formulation [21].

2.1 Modal selection criterion

The limitation on the number of retained modes, constrained by the number of available strain measures ($S > M$), leads to the problem of finding a modal selection criterion. It is fundamental that the retained modes are capable of representing the static deformation that the structure experiences under the load configuration of interest.
Following the procedure described by Bogert et al. [13], it is possible to calculate the least-square fit of the modal coordinates to the static solution with a limited number of retained modes (M_r) and consequently non-squared modal matrix, $[\boldsymbol{\Phi}_{dr}]_{DxM_r}$. Pseudo-inverting $\boldsymbol{\Phi}_{dr}$ in Eq. 1 gives the possibility to compute the approximated modal coordinates $\boldsymbol{q}_r$ that can best represent, in a least-square sense, the static deformed shape $\boldsymbol{w}$ using a

limited number of modes.

$$\boldsymbol{q}_r = (\boldsymbol{\Phi}_{dr}^T \boldsymbol{\Phi}_{dr})^{-1} \boldsymbol{\Phi}_{dr}^T \boldsymbol{w} \tag{7}$$

Using the least-square approximated modal coordinates $\boldsymbol{q}_r$ in Eq. 1, it is possible to compute the approximated modal representation of the static solution $\boldsymbol{w}_r$ using only the retained modes

$$\boldsymbol{w}_r = \boldsymbol{\Phi}_{dr} \boldsymbol{q}_r \tag{8}$$

The modal representation of the static solution can be written as the summation of the contribution of each mode

$$\boldsymbol{w}_r = \sum_{i=1}^{M_r} \boldsymbol{\Phi}_{dr_i} q_{r_i} \tag{9}$$

where $\boldsymbol{\Phi}_{dr_i}$ is the i-th column of the $\boldsymbol{\Phi}_{dr}$ matrix and q_{r_i} is the i-th modal coordinate.
Therefore, the contribution of the i-th mode shape to the total modal representation is

$$\boldsymbol{w}_{r_i} = \boldsymbol{\Phi}_{dr_i} q_{r_i} \tag{10}$$

The strain energy associated with the i-th modal representation of the static deformation is

$$E_{r_i} = \frac{1}{2} \boldsymbol{w}_{r_i}^T \boldsymbol{K} \boldsymbol{w}_{r_i} \tag{11}$$

where $\boldsymbol{K}$ is the stiffness matrix.
Substituting Eq. 10 into Eq. 11 yields

$$E_{r_i} = \frac{1}{2} \, q_{r_i}^T \, \boldsymbol{\Phi}_{dr_i}^T \boldsymbol{K} \boldsymbol{\Phi}_{dr_i} \, q_{r_i} \tag{12}$$

if modal shapes are normalized with respect to mass matrix

$$\boldsymbol{\Phi}_{dr_i}^T \boldsymbol{K} \boldsymbol{\Phi}_{dr_i} = \omega_i^2 \tag{13}$$

where ω_i is the natural angular frequency associated to the i-th mode, Eq. 12 becomes

$$E_{r_i} = \frac{1}{2} \omega_i^2 \, q_{r_i}^2 \tag{14}$$

Comparing the strain energy contribution of each mode with the total strain energy due to the static deformation

$$E = \frac{1}{2} \boldsymbol{w}^T \boldsymbol{K} \boldsymbol{w} \tag{15}$$

it is possible to evaluate how much each mode and the summation of the retained modes is capable of representing the static deformation. Therefore, a selection criterion based on the strain energy contribution is easily obtained.

3 Ko's Displacement theory

Ko's Displacement theory exploits the Bernoulli-Euler beam theory to calculate the deflection and curvature of a beam-like structure along a line where strains are measured.
According to the Bernoulli-Euler theory, the axial strain and the second derivative of the deflection along a longitudinal coordinate p are correlated by the equation:

$$\varepsilon_{pp}(p) = -z w_{,pp}(p) \tag{16}$$

where z is the distance between the neutral axis and the strain sensor.
Since the strain in the current paragraph is always measured along the coordinate p, the subscript pp will be omitted in the rest of the paragraph for notation simplicity.
If axial strain is evaluated at $(N+1)$ discrete p_i locations and it is assumed to be linear between two consecutive locations along p, it is possible to evaluate the axial strain as a function of the coordinate p:

$$\varepsilon(p) = \varepsilon_{i-1} + \frac{(\varepsilon_i - \varepsilon_{i-1})}{(p_i - p_{i-1})}(p - p_{i-1}), \quad p_{i-1} \leq p \leq p_i \quad (i = 1, 2, ...N) \tag{17}$$

The double integration of $\varepsilon(p)$ with respect to p leads to the following expression of the deflection at the i-th discrete sensing point along the measurement line [49]

$$w_i = -\frac{1}{6z}\left[\sum_{j=1}^{i}(2\varepsilon_{j-1} + \varepsilon_j)(p_j - p_{j-1})^2 + 3\sum_{k=1}^{i-1}(\varepsilon_{k-1} + \varepsilon_k)(p_k - p_{k-1})(p_i - p_k)\right] \quad (i = 1, 2, ..., N) \tag{18}$$

Since Ko's displacement theory was developed for the application on wings structures, the cantilevered beam configuration was the one the theory was developed for. Therefore, clamped end boundary conditions ($w(p = 0) = w(p = p_0) = 0$ and $w_{,p}(p = 0) = w_{,p}(p = p_0) = 0$) have to be taken into account to obtain Eq. 18.
The Eq. 18 is valid for measurement points located at a constant distance from the neutral axis. This case is suitable for the application of the present article. Other more general formulations that take into account the variability of z have also been established [8, 9].
As described so far, the Ko's displacement theory is able to evaluate the deflection only at the same location where the strains are measured. In case of torsional deformation, the method can also be applied to roughly estimate twist angle distribution along the chord of the wing-like structure. To achieve that, it is needed to compute the difference between vertical deflection of different lines located at known distance along the chord.

3.1 Extension

Pak developed a method able to further extend the applicability of the Ko displacement's theory [50]. Thanks to a modal expansion process, the method is therefore capable to extend its capabilities to every degree of freedom (DOF), in points different from the ones where the strains sensors are.
To apply the transformation, it is necessary to split the vector of the investigated DOFs into two groups, master DOFs and slave DOFs. The ones that are calculated applying the standard Ko's displacement theory are defined as master ($\boldsymbol{w}_m$) those which it is desired to expand the method to are defined as slave ($\boldsymbol{w}_s$).

$$\boldsymbol{w} = \begin{Bmatrix} \boldsymbol{w}_m \\ \boldsymbol{w}_s \end{Bmatrix} \tag{19}$$

Once the slave and master DOFs are defined, a transformation that expresses both in terms of only the master ones can be adopted

$$\begin{Bmatrix} \boldsymbol{w}_m \\ \boldsymbol{w}_s \end{Bmatrix} = \boldsymbol{T}\boldsymbol{w}_m \tag{20}$$

Through the System Equivalent Reduction and Expansion Process (SEREP) [51] it is possible to define the modal transformation matrix in terms of the master DOFs modal shapes matrix, $[\boldsymbol{\Phi}_{dm}]_{D_m x M}$ and the slave DOFs modal shapes matrix, $[\boldsymbol{\Phi}_{ds}]_{D_s x M}$, where D_m is the number of master DOFs, D_s is the number of slave DOFs and M is the number of the retained modes. The two matrices are computed so that the i-th column of the matrix contains the value of the i-th shape mode correspondent to the master or slave degrees of freedom according to which matrix the construction refers to

$$\boldsymbol{T} = \begin{bmatrix} \boldsymbol{\Phi}_{dm}(\boldsymbol{\Phi}_{dm}^T\boldsymbol{\Phi}_{dm})^{-1}\boldsymbol{\Phi}_{dm}^T \\ \boldsymbol{\Phi}_{ds}(\boldsymbol{\Phi}_{dm}^T\boldsymbol{\Phi}_{dm})^{-1}\boldsymbol{\Phi}_{dm}^T \end{bmatrix} \tag{21}$$

The use of SERP can therefore allow the calculation of every desired DOF starting from discrete strains measurements. This kind of extension applied to the Ko's Displacement theory improves the method but on the other hand adds complexity in terms of required knowledge of the problem's features. In fact, the knowledge of the modal shapes become compulsory when this process is to be applied.
The same criterion previously applied (Sec. 2.1) for the selection of the modes to retain can be used for the construction of the modal shapes matrices adopted by the SERP.
In the following of this paper, for simplicity, reference will always be made to Ko's displacements theory although it should always be considered the extended version of the method as described in this paragraph.

4 iFEM

Starting from the same direct FEM approach, the inverse FEM requires the discretization of the structural domain with finite elements. Consequently, the kinematic variables inside each finite element are interpolated from the nodal degrees of freedom values using shape functions. Finally, the displacement field is expressed in terms of the kinematic variables according to a specific structural theory. Similarly to what happens for the direct FEM, several structural models and theories are available for the development of inverse finite elements, ranging from the Timoshenko beam theory [30] to the Mindlin plate theory [45] and the Refined Zigzag Theory [29, 35, 36]. Considering that the numerical application considered in this paper is a composite wing box with thin-walled components (skin, spars, stringers, ribs) and with a quasi-isotropic stacking sequence (refer to Section 5.1), the Mindlin theory is considered to be adequate. In the following, the description of the iFEM formulation will be introduced for a specific inverse element type based on Mindlin theory. Nonetheless, the described iFEM approach is valid for different theories and elements.
The structural theory for plates adopted throughout this paper is the First order Shear Deformation Theory (FSDT). According to this theory, the displacement field, coherent with the notation of Fig. 1, is

$$u_x(x,y,z) \equiv u_x = u + z\theta_y \tag{22a}$$

$$u_y(x,y,z) \equiv u_y = v - z\theta_x \tag{22b}$$

$$u_z(x,y,z) \equiv u_z = w \tag{22c}$$

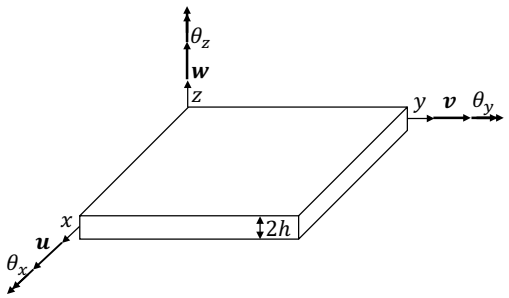

Figure 1: Plate notation.

where u_x, u_y, u_z are the displacement components along the coordinate axes (x, y, z), u and v are the plate mid-surface in-plane displacements, w is the transverse deflection, θ_x and θ_y are the bending rotations.
The structural domain is discretized using iQS4 four-node 2D inverse elements [32]. The formulation of iQS4 element, in terms of shape functions, is the same adopted in the MIN4 element developed by Tessler and Hughes [53]. Moreover, to improve the membrane behavior of the element, the hierarchical drilling DOF, as described by Cook [54], has been introduced in the formulation. Consequently, the element has 3 translational and 3 rotational DOFs per node, accounting for a total of 24 DOFs. The elemental DOFs vector $\mathbf{u}^e$ is then formulated as follows

$$\mathbf{u}^e = [\ \mathbf{u}_1^e\ \mathbf{u}_2^e\ \mathbf{u}_3^e\ \mathbf{u}_4^e\ ]^T \tag{23a}$$

$$\mathbf{u}_i^e = [\ u_i\ v_i\ w_i\ \theta_{xi}\ \theta_{yi}\ \theta_{zi}\ ] \qquad (i = 1, 2, 3, 4) \tag{23b}$$

The in-plane displacements are interpolated with bi-linear shape functions with respect to the nodal in-plane DOFs, whereas a parabolic interpolation involving the drilling nodal degrees of freedom is added

$$u(x, y) = \sum_{i=1}^{4} N_i u_i + \sum_{i=1}^{4} L_i \theta_{zi} \tag{24a}$$

$$v(x, y) = \sum_{i=1}^{4} N_i v_i + \sum_{i=1}^{4} M_i \theta_{zi} \tag{24b}$$

The transverse displacement and the two bending rotations are interpolated using the same anisoparametric functions of the MIN4 element, using both linear (N_i) and parabolic (L_i and M_i) functions

$$w(x, y) = \sum_{i=1}^{4} N_i w_i - \sum_{i=1}^{4} L_i \theta_{xi} - \sum_{i=1}^{4} M_i \theta_{yi} \tag{25a}$$

$$\theta_x(x, y) = \sum_{i=1}^{4} N_i \theta_{xi} \tag{25b}$$

$$\theta_y(x, y) = \sum_{i=1}^{4} N_i \theta_{yi} \tag{25c}$$

The detailed expressions of the shape functions L_i, N_i and M_i can be found in [32].
It is possible to express the strains in terms of the nodal degrees of freedom as follows

$$\begin{Bmatrix} \varepsilon_{xx} \\ \varepsilon_{yy} \\ \gamma_{xy} \end{Bmatrix} = \begin{Bmatrix} u_{,x} \\ v_{,x} \\ v_{,x} + u_{,y} \end{Bmatrix} + z \begin{Bmatrix} \theta_{y,x} \\ -\theta_{x,y} \\ (\theta_{y,y} - \theta_{x,x}) \end{Bmatrix} = \mathbf{e}(\mathbf{u}^e) + z\mathbf{k}(\mathbf{u}^e) = \mathbf{B}^m\mathbf{u}^e + z\mathbf{B}^b\mathbf{u}^e \tag{26a}$$

$$\begin{Bmatrix} \gamma_{xz} \\ \gamma_{yz} \end{Bmatrix} = \begin{Bmatrix} w_{,x} + \theta_y \\ w_{,y} - \theta_x \end{Bmatrix} = \mathbf{g}(\mathbf{u}^e) = \mathbf{B}^s\mathbf{u}^e \tag{26b}$$

where $\mathbf{B}^m$, $\mathbf{B}^b$ and $\mathbf{B}^s$ are the matrices containing the derivatives of the shape functions related to the strain measures $\mathbf{e}$, $\mathbf{k}$ and $\mathbf{g}$, respectively. These strains measures represent the membrane strains, bending curvatures and transverse shear strains of the element, respectively.
The aim of the iFEM is to reconstruct the displacement field that minimizes the error between the strains generated from the reconstructed displacements and the actually measured ones. Therefore, an error functional has to be defined.
The error is expressed by means of a weighted least-square functional that takes into account the error for each one of the strain components. Following the method guidelines, the functional Ψ_e for each element is then formulated

$$\Psi_e(\mathbf{u}^e) = \lambda_e \left\|\mathbf{e}(\mathbf{u}^e) - \mathbf{e}^\varepsilon\right\|^2 + \lambda_k \left\|\mathbf{k}(\mathbf{u}^e) - \mathbf{k}^\varepsilon\right\|^2 + \lambda_g \left\|\mathbf{g}(\mathbf{u}^e) - \mathbf{g}^\varepsilon\right\|^2 \tag{27}$$

where superscript ε denotes the strains measures evaluated from experimentally measured strains and $\mathbf{e}(\mathbf{u}^e)$, $\mathbf{k}(\mathbf{u}^e)$, and $\mathbf{g}(\mathbf{u}^e)$ are the analytical strain measures expressed in terms of the nodal degrees of freedom.
The coefficients λ in Eq. 27 serve as penalty factors to take into account for the presence or absence of the strain measures within the element. Since the transverse shear strains can not be measured, the transverse shear contribution to the functional is always penalized, $\lambda_g = 10^{-4}$. In the case that an element has no measurements, all the members of Eq. 27 are penalized using $\lambda_e = \lambda_k = \lambda_g = 10^{-4}$. On the contrary, when strain measures within an element are available, the weighting factors λ_e and λ_k are set to 1. More in general, if one single measure is present or absent, the correspondent λ coefficient is set to 1 or 10^{-4}.
In case of existing strain measures, the squared norms in Eq. 27 are given as

$$\left\|\mathbf{e}(\mathbf{u}^e) - \mathbf{e}^\varepsilon\right\|^2 = \iint_{A^e} \left(\mathbf{e}(\mathbf{u}^e) - \mathbf{e}^\varepsilon\right)^2 dxdy \tag{28a}$$

$$\left\|\mathbf{k}(\mathbf{u}^e) - \mathbf{k}^\varepsilon\right\|^2 = (2h)^2 \iint_{A^e} \left(\mathbf{k}(\mathbf{u}^e) - \mathbf{k}^\varepsilon\right)^2 dxdy \tag{28b}$$

where h is the half-thickness of the plate and A^e is the area of the element.
In case of absence of measures, the squared norms in Eq. 27 are computed as follows

$$\left\|\mathbf{e}(\mathbf{u}^e)\right\|^2 = \iint_{A^e} \mathbf{e}(\mathbf{u}^e)^2 dxdy \tag{29a}$$

$$\left\|\mathbf{k}(\mathbf{u}^e)\right\|^2 = (2h)^2 \iint_{A^e} \mathbf{k}(\mathbf{u}^e)^2 dxdy \tag{29b}$$

$$\left\|\mathbf{g}(\mathbf{u}^e)\right\|^2 = \iint_{A^e} \mathbf{g}(\mathbf{u}^e)^2 dxdy \tag{29c}$$

Once the error functional is computed, it has to be minimized with respect to the nodal degrees of freedom. This leads to the system of linear equations typical of the finite elements problem

$$\frac{\partial \Psi_e(\mathbf{u}^e)}{\partial \mathbf{u}^e} = \mathbf{k}^e \mathbf{u}^e - \mathbf{f}^e = 0 \tag{30a}$$

$$\mathbf{u}^e = \mathbf{k}^{e\,-1} \mathbf{f}^e \tag{30b}$$

The problem is completed by operating a standard finite element assembly procedure over all the elements of the structure. In fact, from the local matrices and vectors it is possible to evaluate the global coefficients matrix $\mathbf{K}$ and the global vector of known terms $\mathbf{F}$ and therefore calculate the vector of the global degrees of freedom of the structure $\mathbf{U}$ (after imposing the boundary conditions)

$$\mathbf{U} = \mathbf{K}^{-1} \mathbf{F} \tag{31}$$

The method's input data relative to membrane strains ($\mathbf{e}_i^\varepsilon$) and bending curvatures ($\mathbf{k}_i^\varepsilon$) can be easily computed from experimentally measured surface strains at the i-th point location (Figure 2) [45]. These input data can be evaluated measuring the surface strains on top and bottom surface of the plate

$$\mathbf{e}_i^\varepsilon = \frac{1}{2} \begin{Bmatrix} \varepsilon_{xx}^+ + \varepsilon_{xx}^- \\ \varepsilon_{yy}^+ + \varepsilon_{yy}^- \\ \gamma_{xy}^+ + \gamma_{xy}^- \end{Bmatrix}_i \tag{32a}$$

$$\mathbf{k}_i^\varepsilon = \frac{1}{2h} \begin{Bmatrix} \varepsilon_{xx}^+ - \varepsilon_{xx}^- \\ \varepsilon_{yy}^+ - \varepsilon_{yy}^- \\ \gamma_{xy}^+ - \gamma_{xy}^- \end{Bmatrix}_i \tag{32b}$$

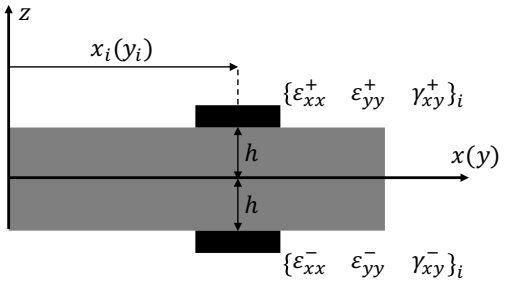

Figure 2: Strains measurements.

The experimental strains measures can be evaluated, thanks to Eq. 32, at a discrete finite number of locations within the elements. Since in Eqs. 28 the strains measures are evaluated on the entire element domain, a method to expand the experimental measure to the entire domain has to be established.

4.1 Single strain smoothing

In typical finite elements applications, the integrals are calculated numerically. In particular, the Gauss quadrature is commonly used. By using this technique, the integrals in Eqs. 28 are transformed into summations of the function over the nxn Gauss points multiplied by the corresponding ω_i quadrature weights. Consequently, to exactly perform the squared norms, at least nxn strain measurements for each element are required.
To reduce the number of measurements to only one, the same smoothing approach used for the functional in case of missing strain data has been introduced. Considering that for odd number of Gauss points there is always a Gauss point located at the centroid of the element, only one measure at centroid location of each sensorized element has been considered. Then, weighting factors χ_i within the Gauss summation have been

introduced [55]. As for the aforementioned smoothing technique, a penalty factor of $\chi = 10^-4$ has been associated to the Gauss points without measures, while a factor of $\chi = 1$ has been associated to the centroid.
The novel approach modifies the integrals in Eqs. 28 as follows

$$\left.\begin{aligned} \|\mathbf{e}(\mathbf{u}^e) - \mathbf{e}^\varepsilon\|^2 &= \sum_{i=1}^{nxn} \chi_i \omega_i \left(\mathbf{e}(\mathbf{u}^e)_i - \mathbf{e}_i^\varepsilon\right)^2 \\ \|\mathbf{k}(\mathbf{u}^e) - \mathbf{k}^\varepsilon\|^2 &= (2h)^2 \sum_{i=1}^{nxn} \chi_i \omega_i \left(\mathbf{k}(\mathbf{u}^e)_i - \mathbf{k}_i^\varepsilon\right)^2 \end{aligned}\right\} \begin{pmatrix} \chi_{i=centroid} = 1 \\ \chi_{i\neq centroid} = 10^{-4} \end{pmatrix} \tag{33}$$

5 Numerical analysis

The three methods mentioned above were numerically tested and compared on a rectangular composite wing box. The reference displacements and the relative strains for the application of the methods were calculated from a high-fidelity direct FE model, using the commercial FEM code MSC/NASTRAN®. For the computation of the modal shapes, necessary for the application of the Modal and Ko methods, the same model was used. An optimization of the sensor positioning for all the three methods was conducted in order to compare the three techniques performing each at its own best possibilities.

5.1 Test case

The test case analyzed was a composite wing box with a constant rectangular cross-section along the wing span. The wing span length considered was 1600 mm, while the cross-section was characterized by a height of 201 mm and a chord of 667 mm. The wing box presented four T-shaped stringers located two on the top and two on the bottom panel and its wing span was divided into three bays by two rectangular ribs. Four stiffeners were used in the corners of the box to connect skin and spars (Fig. 3a).
All the structural components are composite laminates whose lamina characteristics are summarized in Table 1. A quasi-isotropic $(+45/-45/0/90)_s$ stacking sequence was assigned to all the components. The lamina thickness for the skin and spars was set to 0.25 mm while for the other components it was set to 0.2 mm.

$E_{11}[GPa]$	$E_{22}[GPa]$	ν_{12}	$G_{12}[GPa]$
111	7.857	0.34	3.292

Table 1: Lamina characteristics.

The load case considered for the analysis was the following. Root section clamped boundary condition were considered and a distributed trapezoidal load along the chord direction was applied on the upper skin at the tip section, as showed in Fig. 3b, where $q = 16\ N/mm$. The investigated deformation that resulted from this load case showed both bending and torsional components.

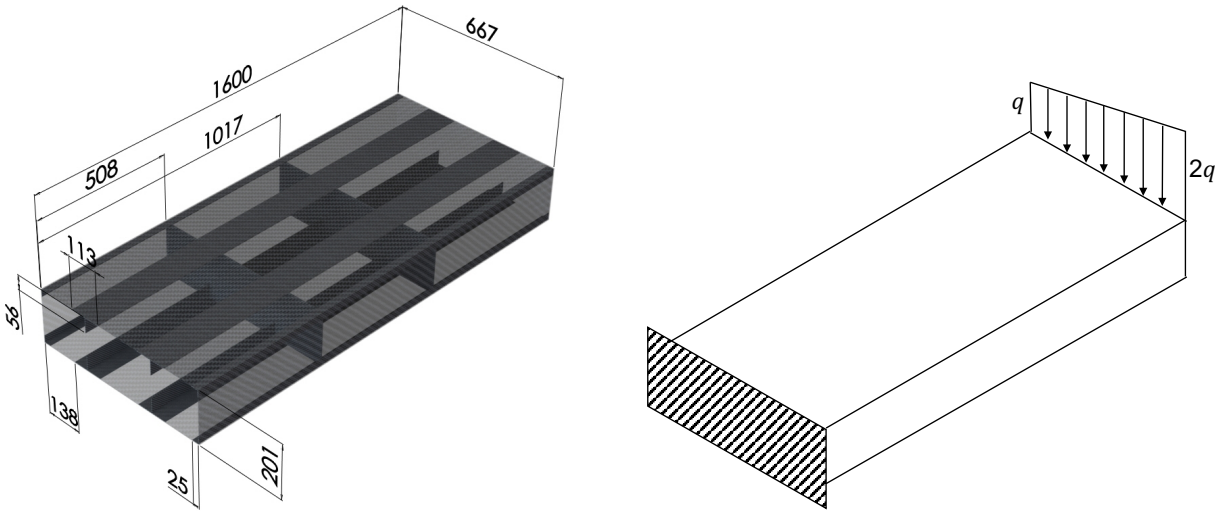

a) Geometry b) Boundary conditions

Figure 3: Wing box.

5.2 Models

Two models of the structure were realized. A high-fidelity reference FE model and an inverse FE model.
The high-fidelity model is constituted of 21004 CQUAD4 NASTRAN® elements and 16027 nodes (Fig. 4a). The use of plate elements based on Mindlin theory is considered to be accurate since the wing box is made of quasi-isotropic and thin-walled components. Moreover, the mesh pattern and the number of CQUAD4 elements have shown to provide convergent results.
The data for the investigated deformed shape were retrieved from the direct analysis of this model. More in details, the reference value for the reconstruction of the displacements and the input strains for the application of the three methods were calculated with the high-fidelity FE model. The modal characteristics of the structures were also computed using this model. The results of the modal analysis will be discussed more in details in the next paragraph.
The inverse model was realized using a coarser mesh of 1427 iQS4 quad elements and 1064 nodes (Fig. 4b). The requirement of a coarser mesh for iFEM is due to the fact that a good ratio between sensorized and unsensorized elements is necessary. A finer mesh, although capable of better representing the deformation, would require a larger number of sensors.

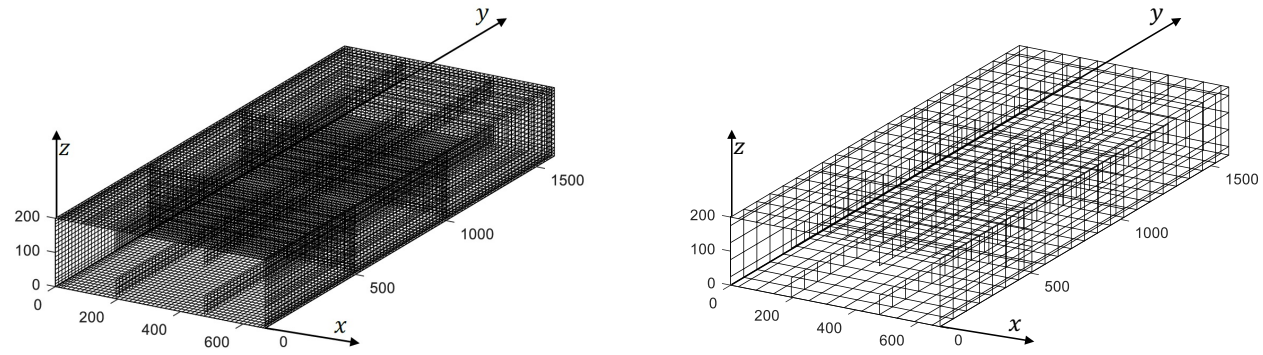

a) High fidelity FEM b) iFEM

Figure 4: Models.

The two models have some compatibility characteristics necessary to compare the iFEM solution with the reference one and to correctly attribute the input strains to the inverse finite element method. All the nodes of the iFEM model have a corresponding node in the FE model, so that a comparison between the nodal displacements can be performed. Moreover, the centroids of the inverse element are located where the FE mesh has a node. Thanks to this correlation it is immediate to attribute the nodal strain from the FE solution to the corresponding elements of the iFE model, according to the single strain smoothing technique (Sec. 4.1).

5.3 Modes selection

The modal analysis was developed using the high-fidelity model. The first 50 mode shapes were calculated with the NASTRAN®'s SOL 103. Once the mode shapes were evaluated, the strain energy contribution to the static deformation's strain energy of each mode shape was computed (Sec. 2.1). The mode shapes from 31 to 50 were discarded because of the low level of reliability the numerical high frequency mode have. The first 30 modes are able to represent the 90.7% of the total deformation strain energy. Within the selected range of the first 30 modes, the modes that contribute most to the total strain energy are the 1st, 3rd and 26th, as shown in Fig. 5. The summation of these three modes contributes to the total strain energy for the 89.7%. Therefore, these modes were selected for the construction of the modal matrices necessary for the application of the Modal Method and for the extension of the Ko's Displacement theory.

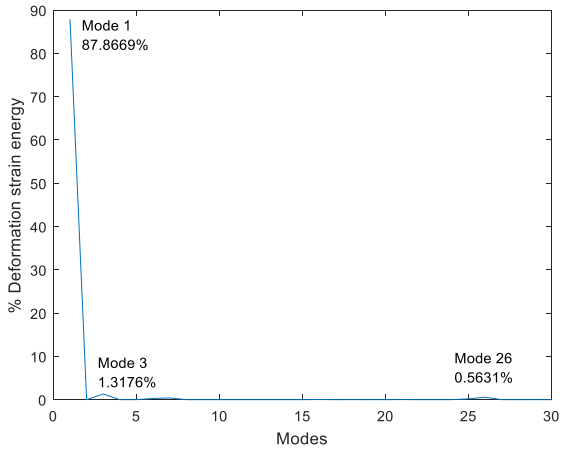

Figure 5: Modes contribution to the total deformation strain energy.

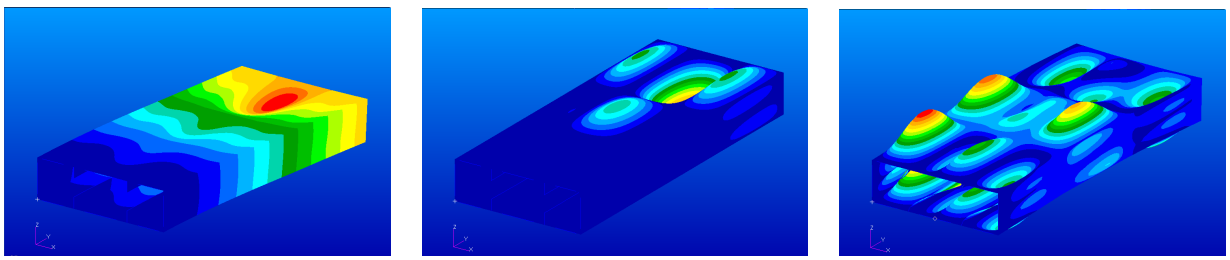

a) Mode 1 b) Mode 3 c) Mode 26

Figure 6: Selected mode shapes.

5.4 Strain sensors optimization

The three methods' performance strongly depend on the number and position of the strains information that are provided to them. In order to make a consistent comparison of the three methods, it was chosen to compare them when performing in their optimum condition with a limited number of sensors. Therefore, the best strains sensors locations and directions, using a fixed number of sensors, were investigated for each technique.
The investigation over the best sensors configuration can be expressed as the search for the configuration

that minimizes the value of the error between the reconstructed and the reference deformation. The solution landscape, that represents the different solutions for the different configurations, can result really complex and rugged, with multiple local minima values of the error. This kind of solution landscapes are particularly suited to be explored with a genetic algorithm optimizer. Moreover, genetic algorithms have been already successfully applied to the study of the sensors configuration for shape sensing by Foss and Haugse in [15]. As a consequence, also in this work, the sensors configuration investigation was carried on using a genetic algorithm optimizer.
The optimizer operated in two selection phases. During the first one, a selection criterion based on the individual fitness value was adopted. During the second one, a selection criterion based on the individual ranking was used. The first phase is capable of a broader search that helps to not get stuck in local optima whereas the second phase is capable of increasing the selective pressure towards the best configuration, only after the broader search is accomplished. Both phases were stopped when no significant increase in the objective function was observed over 10 generations. Each generation comprised a population of 500 individuals and within each generation, the one-point crossover, the two-points crossover, the mutation and the permutation genetic operators have been applied with a probability of 1, 0.9, 0.001 and 0.001 respectively.
The detailed description of the optimization parameters will be provided in the next sections.

5.4.1 Objective

The objective of the optimization was to minimize the root mean square percent error between the displacements along the z direction (Fig. 4) of the high-fidelity FEM (w^{ref}) and the ones reconstructed with the three methods (w):

$$\%ERMS_w = 100 \times \sqrt{\frac{1}{n}\sum_{i=1}^{n}\left(\frac{w_i - w_i^{ref}}{w_{max}^{ref}}\right)^2} \tag{34}$$

where w_{max}^{ref} is the maximum value of the reference vertical displacements. The vertical displacements were considered because they are related to the main global deformation of the wing box.
In order to perform a consistent comparison, for every method, the vertical displacements, and consequently the $\%ERMS_w$, were calculated over the n nodes that the iFEM mesh and the reference mesh have in common.

5.4.2 Variables

As previously noted, the aim of the optimization was to find the best sensors configuration for the three methods. As a consequence, the optimization variables for this problem were the sensors location and the kind of strain measured by the sensor. The kind of measurement is defined by the strain component or the strains components measured by the sensor.
Since the Ko's Displacements theory is formulated for strains along the wingspan direction, the only type of sensor admitted in the optimization was the single component strain gauge in that direction. On the other hand, the iFEM and MM can admit different direction strain measurements. Therefore, the optimizer could select two type of sensors, the single component strain gauge and the 3 components rosette.
The number of sensors was initially established in 108 units and could not be directly changed during the optimization process. Nevertheless, the possibility to select one sensor more than once, and consequently decrease the total number of information actually used, was left.
Summarizing, the optimization process consisted in selecting 108 sensors for each method. For the Ko's Displacement theory this resulted in a maximum of 108 single strain gauges. For the iFEM and MM it resulted in a minimum of 108 single strain gauges and maximum of 108 strain rosettes, accounting for a maximum of 324 single strain measures. The selected number of sensors could be decreased for each method if some sensors were picked more than once by the optimizing algorithm.

5.4.3 Sensors search space

The search for the optimum sensors locations was performed selecting them between a limited number of possible positions. As for the evaluation of the $ERMS_w$, the iFEM model is the one that somehow limited the sensors search space. In fact, the iFEM method, using the approach described in (Sec.4.1), only admit one sensor in the centroid of each element. Therefore, the admissible sensors positions are the ones that lay in the centroid of the inverse elements.

Considering the practical difficulties connected to the application of sensors inside the wing box, only strains measured on the external surface were considered. Therefore, for the computation of the strain measures in Eqs. 32, constant values of the strains through the thickness of each plate were considered. This approximation is admissible if the thickness of the skin panels is considerably smaller than the one of the entire wing box. In that case, the variation of the strains through the plate thickness can be considered negligible with respect to the variation of the strains through the entire wing box. As a consequence, the areas were structural components overlap were not considered part of the sensors search space because of the resulting increase in the global plate thickness.

Given the previous considerations, the resulting variables search spaces for the optimization algorithm are showed in Fig. 7 for lower and upper skins and in Fig. 8 for front and rear spars.

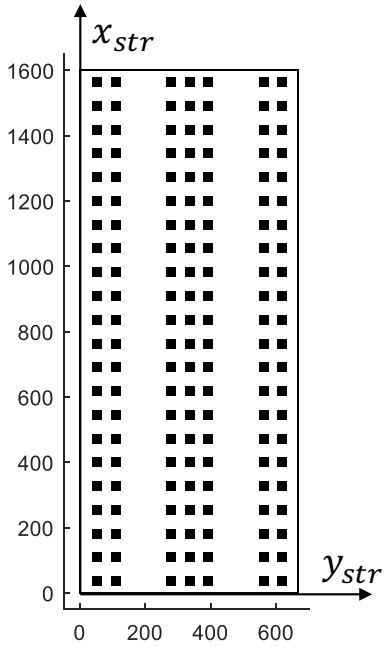

Figure 7: Skins sensors search space.

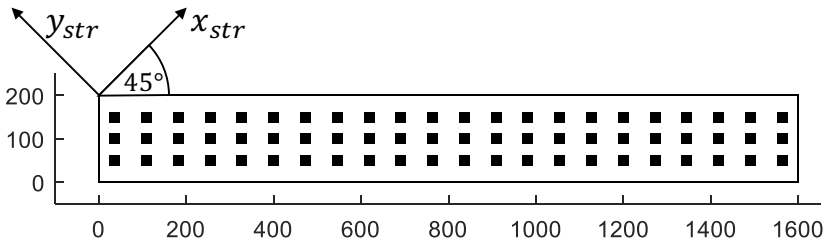

Figure 8: Spars sensors search space.

The Ko Displacement's theory was applied considering the entire wing box as a beam-like structure. Consequently, the only considered strains for this method were the one from the upper and lower skins (Fig. 7).

According to the method's prescriptions, only the strains in the wingspan direction $\varepsilon_{x_{st}}$ were considered.
For iFEM and MM all the positions showed in both the skins and the spars were allowable. For each position either single strain gauge, measuring the strain along the wingspan direction $\varepsilon_{x_{st}}$, or strain rosettes, measuring the three strain components $\varepsilon_{x_{st}}$, $\varepsilon_{y_{st}}$ and $\gamma_{x_{st}y_{st}}$, were considered. The strains sensors directions on the spars were inclined by 45 degrees to better catch the shear deformation that these components typically experience.

5.5 Results

The results of the optimization in terms of $ERMS_w$ and number of selected sensors are summarized in the following table:

	Ko	**MM**	**iFEM**
$ERMS_u$ [%]	49.9	62.3	**15.8**
$ERMS_v$ [%]	11.8	8.4	**4.3**
$ERMS_w$ [%]	6.9	4.8	**1.8**
S_x	28	27	
R_{xy}		45	108
S_{tot}	**28**	162	324

Table 2: Optimization results.

The numbers of single strain sensors (S_x), strain rosettes (R_{xy}) and total strain measurement (S_{tot}), reported in Table 2, are referred to the real number of sensors used in the application of each method, removing the repeated sensors that the optimizer selected. In Table 2, the $ERMSs$ are also reported for the displacements along the x direction ($ERMS_u$) and along the y direction ($ERMS_v$). As already explained in Section 5.4.1, the vertical displacements are the prevalent ones in this application, therefore, the $ERMS_w$ is used as the primary variable to assess the accuracy of the shape reconstructions. Moreover, when analyzing the errors of the reconstruction along x and y, it is important to take into account that the sensors configurations have not been optimized in order to minimize these values, but the ones along z.
The sensors distribution for the configurations described in the table and the resulting reconstructed deformations are plotted in Figs. 9-14. Figure 15 shows the deflections, computed with the three methods and with the high-fidelity Finite Element reference model, of a line of nodes belonging to the lower panel and located close to the mid-chord position ($x = 363.182$).
The best accuracy, with respect to the $ERMSs$ along all the three directions, is obtained by the **iFEM** method. An $ERMS_w$ slightly below 2% is observed. The optimization process, in this case, selected the maximum number of sensors to reach this value of the error. As showed in Fig. 10, the rosettes are all positioned on the spars of the wing box. The resulting reconstructed deformation doesn't show large discrepancy with respect to the reference one.
On the other hand, the **Ko's Displacement theory's** results were obtained with a low number of sensors selected by the optimizer to reach a modest 6.9% value of the $ERMS_w$. The few sensors are located on the lines located as close as possible to the leading and trailing edge of the wing (Fig. 12). The low number of sensors is due to the fact that the optimizer selected many times the same sensors. This behavior was studied in more details. A second optimization was performed, adding a penalization factor to all the solutions with repeated sensors, in order to force the optimizer to select the maximum number of sensors available. The results showed an even poorer $ERMS_w$ value for the optimal solution. A high number of sensors, for this test configuration, seemed to not have a beneficial effect on the evaluation of the vertical displacements in the application of the classical Ko's theory in the first step of the extended procedure. Therefore, a larger number of sensors resulted in a larger number of inaccurate vertical displacements used in the subsequent modal transformation. As a consequence, the transformation somehow amplified the errors from the master DOFs, leading to a higher value

of the global error.
Looking at Fig. 11 is possible to notice some discrepancy between the reconstructed and the reference deformation. Especially in the bay at the tip, it is possible to observe that the reconstructed displacement is strongly biased by the skins' deflection waves of the first mode shape of the structure (Fig. 6). From Fig. 15 it is easy to observe the inaccuracies of the method in the reconstruction of the deflection inside the last two bays and the tendency of the method to reproduce the modal shapes.
A trade-off between the two methods previously described is provided by the **Modal Method**. The method is capable of reaching an acceptable accuracy with a modest number of sensors.
The optimizer selected both single strain sensors and strain rosettes and some repetitions occurred. The distribution of the sensors over the structure doesn't show a recognizable pattern (Fig. 14). A study that avoided the repetition was performed for this method too. In this case, the use of all possible sensors didn't affect the global error. The study suggested that the 4.8% $ERMS_w$ seems to be the maximum accuracy the method is capable to reach, regardless of how many strain measurements and modes are used. In fact, an analysis with the full set of strains measures and including all the 50 computed modes, resulted in the same $ERMS_w$ value of 4.8%, proving that the modes selection and the sensors optimization is capable to reach an asymptotic best value of the error.
The shapes comparison (Fig. 13) and the bottom mid-chord line deflection (Fig. 15) showed the same behavior, although with less intensity, of the Ko's Displacements theory. Deflection waves in the second and third bays' lower and upper panels are observed. These waves are present in the 1st mode shape (Fig. 6) of the structure.

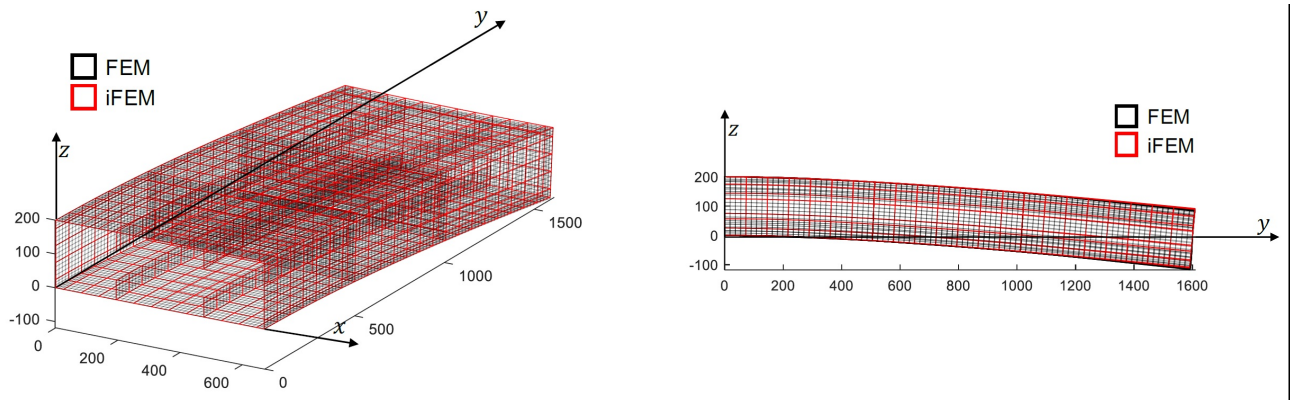

a) isometric view b) lateral view

Figure 9: iFEM shape reconstruction (Scale factor for the displacements = 7).

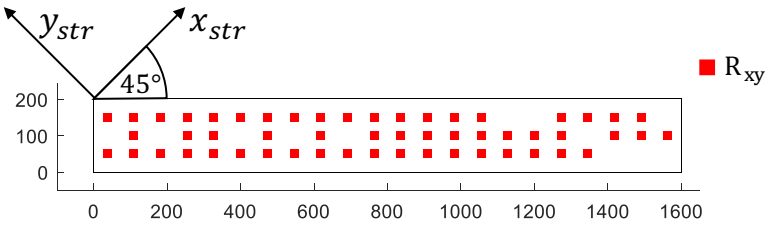

a) front spar ($x = 0$)

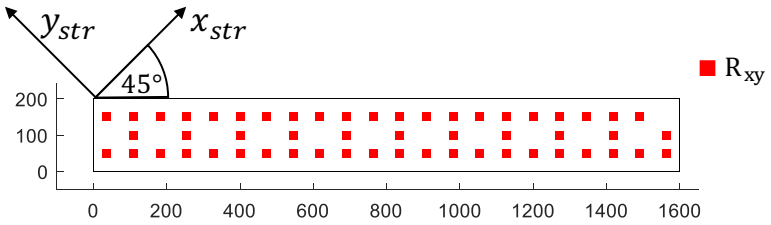

b) rear spar ($x = 670$)

Figure 10: iFEM sensors distribution.

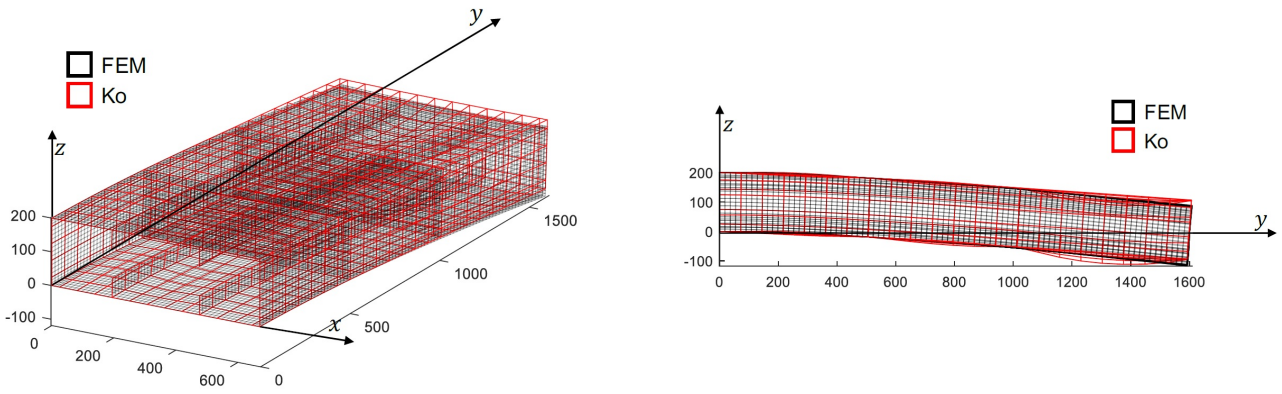

a) isometric view b) lateral view

Figure 11: Ko's displacements theory shape reconstruction (Scale factor for the displacements = 7).

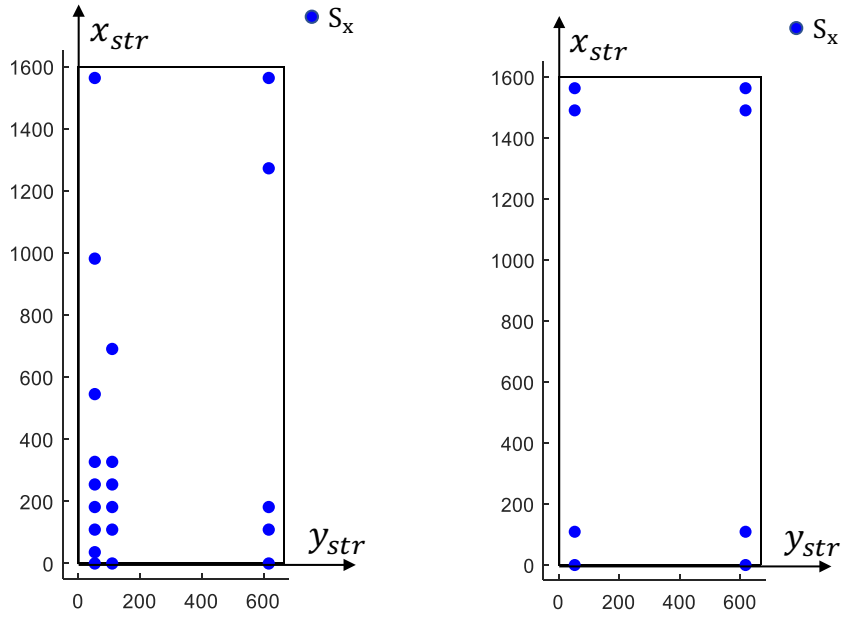

a) upper skin ($z = 201$) b) lower skin ($z = 0$)

Figure 12: Ko's displacements theory sensors distribution.

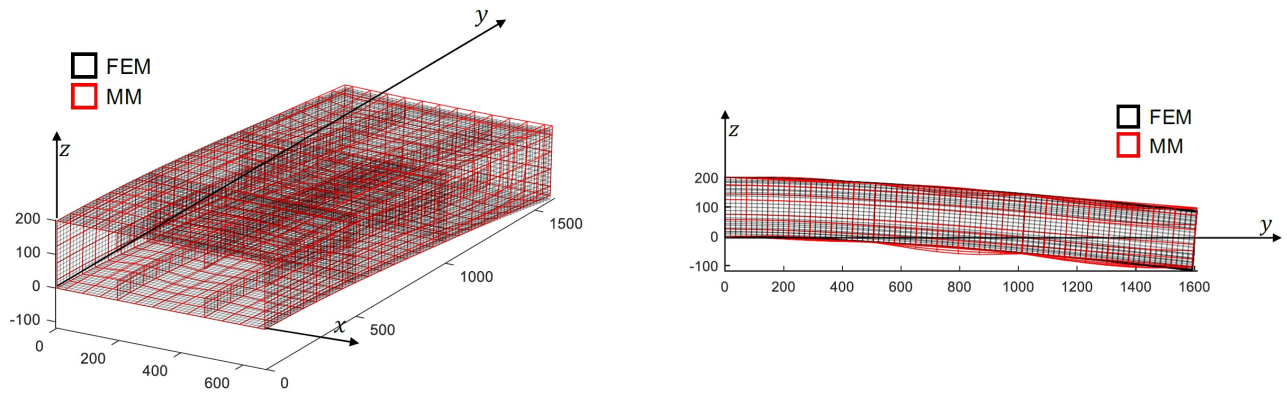

a) isometric view

b) lateral view

Figure 13: Modal Method shape reconstruction (Scale factor for the displacements = 7).

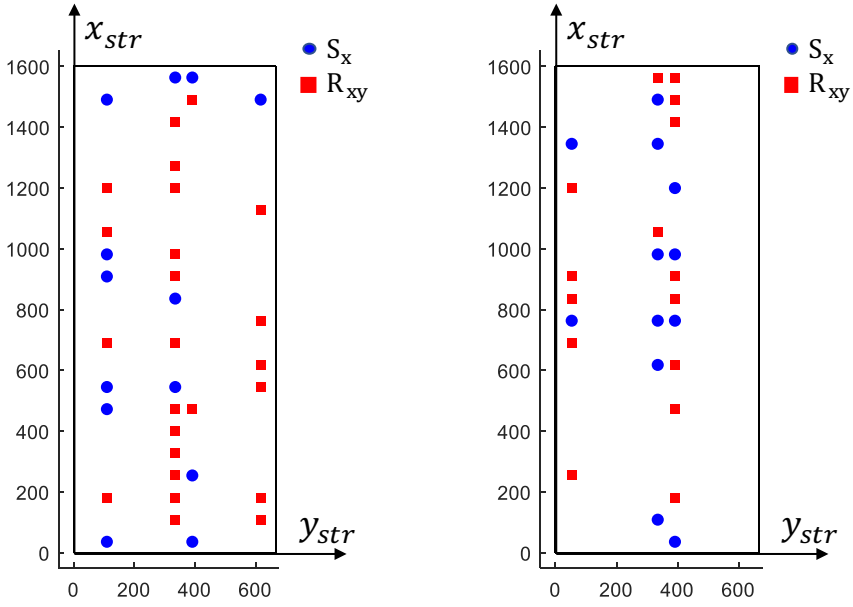

a) upper skin ($z = 201$)

b) lower skin ($z = 0$)

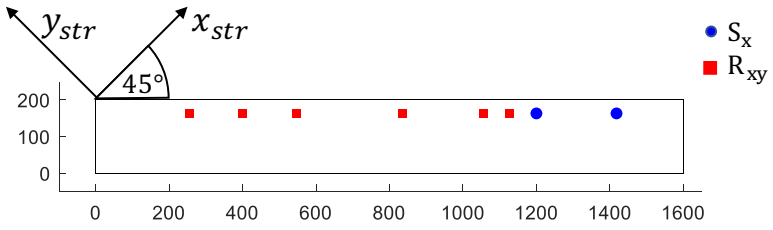

c) rear spar ($x = 670$)

Figure 14: Modal Method sensors distribution.

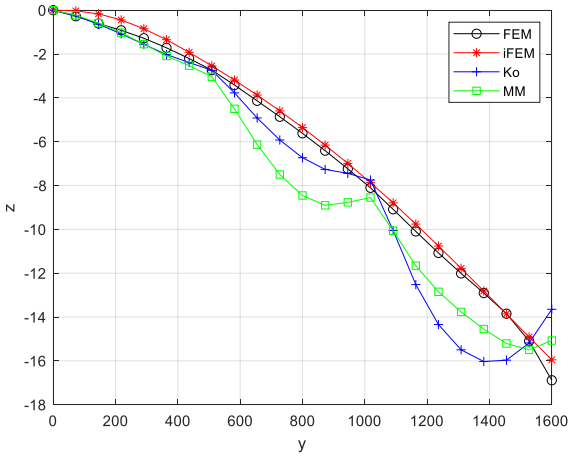

Figure 15: Vertical displacement along the mid-chord line ($x = 363.182$) on the bottom panel.

6 Conclusions

This paper compared three shape sensing methods, iFEM, the Modal Method and the Ko's Displacements theory, on a complex structure undergoing a complex deformation, a composite wing box subjected to bending and torsion. The methods have been described in details and some modifications to the classical formulations have been discussed. In particular, an extension of the Ko's Displacements theory, that allows to predict displacements in arbitrary positions on the structure, has been described. Moreover, a modified approach, able to increase the reliability regarding the strain association to the iFEM's 4-node elements, has been developed.
The comparison involved an optimization of the sensors configuration that allowed to compare the best performances of each method. The final configurations have been compared evaluating the accuracy to predict the vertical displacements of the whole structure. The number of sensors was established and could be lowered only if it was proven to increase the accuracy of a method.
The iFEM showed to be the more accurate in reconstructing the vertical displacements of the wing box. Although being more accurate, it also required the largest number of sensors to reach its best performance. The Modal Method was able to predict the deformation with acceptable accuracy using less sensors. Finally, the Ko's Displacements theory was able to provide a rough estimation of the deformed shape requiring very few sensors.
To complete the comparison, it has been verified that the use of a higher number of sensors for the Ko's Displacement theory and the Modal method was ineffective or even detrimental for the methods' performances. Therefore, it was demonstrated that even with the same number of sensors they could not reach the level of accuracy obtained by the iFEM.
In conclusion, the methods showed different characteristics that could be useful for different purposes and different requirements. The possibility to have a high number of sensors and the requirement for a high precision suggests the use of the more accurate iFEM method whereas, a scarcity of sensors and the requirement of a first-approximation estimate suggests the use of the Ko's Displacement theory. The Modal Method represents a trade-off between these two methods, being capable of a decent accuracy with a medium number of sensors.
The Modal Method and the Ko's Displacement theory, as formulated in this work, require the knowledge of the modal characteristics of the structure whereas the iFEM doesn't have this requirement. Consequently, a further study on the robustness of the first two methods with respect to uncertainties of the structural characteristics should be considered for a more complete comparison. A sensitive study on the influence of noisy strain data should also be considered for further analysis, as it is a problem to address in the case of real structures applications. Moreover, a more exhaustive study on the influence of the number of sensors on the performance of the three methods should be carried on in future works. In particular, the possibility of virtually expanding fewer sensors' data through interpolation or other techniques should be considered.

Acknowledgments:
Computational resources were provided by HPC@POLITO, a project of Academic Computing within the Department of Control and Computer Engineering at the Politecnico di Torino (http://www.hpc.polito.it)

References

[1] Barbarino, S., Bilgen, O., Ajaj, R., Friswell, M. and Inman, D. (2011) *A Review of Morphing Aircraft.* Journal of Intelligent Material Systems and Structures, 22(9), pp. 823-877.

[2] Evenblij, R., Kong, F., Koimtzoglou, C., Ciminello, M., Dimino, I. and Concilio, A. (2015) *Shape Sensing for Morphing Structures Using Fiber Bragg Grating Technology.* Smart Intelligent Aircraft Structures (SARISTU), Springer, Cham.

[3] Di Sante, R. (2015) *Fibre Optic Sensors for Structural Health Monitoring of Aircraft Composite Structures: Recent Advances and Applications.* Sensors, 15(8), pp. 18666-18713.

[4] Soller, B., Gifford, D., Wolfe, M. and Froggatt, M. (2005) *High resolution optical frequency domain reflectometry for characterization of components and assemblies.* Optics Express, 13(2), pp. 666-674.

[5] Akl, W., Poh, S. and Baz, A. (2007). *Wireless and distributed sensing of the shape of morphing structures.* Sensors and Actuators A: Physical, 140(1), pp. 94-102.

[6] Bakalyar, J. and Jutte, C. (2012) *Validation Tests of Fiber Optic Strain-Based Operational Shape and Load Measurements.* In: Proceedings of the 53rd AIAA/ASME/ASCE/AHS/ASC Structures, Structural Dynamics and Materials Conference, 2012. Honolulu.

[7] Jutte, C.V., Ko, W.L., Stephens, C.A., Bakalyar, J.A. and Richards W.L. (2011) *Deformed Shape Calculation of a Full-Scale Wing Using Fiber Optic Strain Data from a Ground Loads Test.* NASA/TP-2011-215975.

[8] Ko, W.L., Richards, W.L. and Fleischer, V.T. (2007) *Displacement Theories for In-Flight Deformed Shape Predictions of Aerospace Structures.* NASA/TP-2007-214612.

[9] Ko W.L., Richards W.L. and Fleischer V.T. (2009) *Applications of the Ko displacement theory to the deformed shape predictions of the doubly-tapered Ikhana wing.* NASA/TP-2009-214652.

[10] Ko, W.L., Richards, W.L. and Fleischer, V.T. (2009) *Further Development of Ko Displacement Theory for Deformed Shape Predictions of Nonuniform Aerospace Structures.* NASA/TP-2009-214643.

[11] Smoker, J. and Baz, A. (2008) *Monitoring the bending and twist of morphing structures.* Proc. SPIE 6932, Sensors and Smart Structures Technologies for Civil, Mechanical, and Aerospace Systems 2008. San Diego.

[12] Bang, H., Ko, S., Jang, M. and Kim, H. (2012) *Shape estimation and health monitoring of wind turbine tower using a FBG sensor array.* in: Proceedings of the 2012 IEEE International Instrumentation and Measurement Technology Conference, 2012. Graz.

[13] Bogert, P., Haugse, E.D. and Gehrki, R. (2003) *Structural Shape Identification from Experimental Strains Using a Modal Transformation Technique.* in: Proceedings of the 44th AIAA/ASME/ASCE/AHS/ASC Structures, Structural Dynamics, and Materials Conference, 2003. Norfolk..

[14] Davis, M., Kersey, A., Sirkis, J. and Friebele, E. (1996) *Shape and vibration mode sensing using a fiber optic Bragg grating array.* Smart Materials and Structures, 5(6), pp. 759-765.

[15] Foss, G. C. and Haugse, E.D. (1995) *Using Modal Test Results to Develop Strain to Displacement Transformations.* In: Proceedings of the 13th International Conference on Modal Analysis, 1995. Nashville.

[16] Jones, R., Bellemore, D., Berkoff, T., Sirkis, J., Davis, M., Putnam, M., Friebele, E. and Kersey, A. (1998) *Determination of cantilever plate shapes using wavelength division multiplexed fiber Bragg grating sensors and a least-squares strain-fitting algorithm.* Smart Materials and Structures, 7(2), pp. 178-188.

[17] Kang, L., Kim, D. and Han, J. (2007) *Estimation of dynamic structural displacements using fiber Bragg grating strain sensors.* Journal of Sound and Vibration, 305(3), pp. 534-542.

[18] Kim, H., Kang, L. and Han, J. (2011) *Shape estimation with distributed fiber Bragg grating sensors for rotating structures.* Smart Materials and Structures, 20(3), pp. 035011.

[19] Kim, N. and Cho, N. (2004) *Estimating deflection of a simple beam model using fiber optic bragg-grating sensors.* Experimental Mechanics, 44(4), pp. 433-439.

[20] Li, C. and Ulsoy, A. (1999). *High-precision measurement of tool-tip displacement using strain gauges in precision flexible line boring.* Mechanical Systems and Signal Processing, 13(4), pp. 531-546.

[21] Li, L., Zhong, B.S., Geng, Z.Y. and Sun, W. (2017) *Structural Shape Reconstruction of FBG Flexible Plate Using Modal Superposition Method.* In: Proceedings of the International Design Engineering Technical Conferences and Computers and Information in Engineering Conference, 2017. Cleveland.

[22] Lively, P., Atalla, M. and Hagood, N. (2001) *Investigation of filtering techniques applied to the dynamic shape estimation problem.* Smart Materials and Structures, 10(2), pp. 264-272.

[23] Pisoni, A.C., Santolin, C., Hauf, D.E. and Dubowsky, S. (1995) *Displacements in a vibrating body by strain gauge measurements.* In: Proceedings of the 13th International Conference on Modal Analysis, 1995. Nashville.

[24] Rapp, S., Kang, L., Han, J., Mueller, U. and Baier, H. (2009) *Displacement field estimation for a two-dimensional structure using fiberBragg grating sensors.* Smart Materials and Structures, 18(2), pp. 025006.

[25] Yin, W., Fu, T., Liu, J. and Leng, J. (2009) *Structural shape sensing for variable camber wing using FBG sensors.* Proc. SPIE 7292, Sensors and Smart Structures Technologies for Civil, Mechanical, and Aerospace Systems 2009.San Diego.

[26] Alioli, M., Masarati, P. Morandini, M., Carpenter, T., Osterberg, N.B. and Albertani, R. (2017) *Membrane shape and load reconstruction from measurements using inverse Finite Element analysis.* AIAA Journal, 55(1), pp. 297308.

[27] Cerracchio, P., Gherlone, M., Mattone, M., Di Sciuva, M. and Tessler, A. (2010) *Shape sensing of three-dimensional frame structures using the inverse Finite Element Method.* In: Proceedings of the 5th European Workshop on Structural Health Monitoring, 2010. Sorrento.

[28] Cerracchio, P., Gherlone, M. and Tessler, A. (2015) *Real-time displacement monitoring of a composite stiffened panel subjected to mechanical and thermal loads.* Meccanica, 50, pp. 24872496.

[29] Cerracchio, P., Gherlone, M., Di Sciuva, M. and Tessler, A. (2015) *A novel approach for displacement and stress monitoring of sandwich structures based on the inverse Finite element method.* Composite Structures, 127, pp. 6976.

[30] Gherlone, M., Cerracchio, P., Mattone, M., Di Sciuva, M. and Tessler, A. (2012) *Shape sensing of 3D frame structures using an inverse Finite Element Method.* International Journal of Solids and Structures, 49(22), pp. 31003112.

[31] Gherlone, M., Cerracchio, P., Mattone, M., Di Sciuva, M. and Tessler, A. (2014) *Inverse Finite Element Method for beam shape sensing: theoretical framework and experimental validation.* Smart Materials and Structures, 23(4), pp. 045027.

[32] Kefal, A., Oterkus, E., Tessler, A., and Spangler, J.L. (2016) *A quadrilateral inverse-shell element with drilling degrees of freedom for shape sensing and structural health monitoring.* Engineering Science and Technology, an International Journal, 19(3), pp. 12991313.

[33] Kefal A., Oterkus E. (2016) *Displacement and stress monitoring of a chemical tanker based on inverse finite element method.* Ocean Engineering, 112, pp. 3346.

[34] Kefal, A. and Oterkus, E. (2016) *Displacement and stress monitoring of a Panamax containership using inverse finite element method.* Ocean Engineering, 119, pp. 1629.

[35] Kefal, A., Tessler, A., Oterkus, E. (2017) *An enhanced inverse Finite element method for displacement and stress monitoring of multilayered composite and sandwich structures.* Composite Structures, 179, pp. 514540.

[36] Kefal, A., Yildiz, M. (2017) *Modeling of sensor placement strategy for shape sensing and structural health monitoring of a wing-shaped sandwich panel using inverse Finite element method.* Sensors, 17(12), pp. 2775.

[37] Kefal, A., Bunga j.M., Oterkus, E., Yildiz, M. (2018) *Three dimensional shape and stress monitoring of bulk carriers based on iFEM methodology.* Ocean Engineering, 147, pp. 256267.

[38] Kefal, A. (2019) *An efficient curved inverse-shell element for shape sensing and structural health monitoring of cylindrical marine structures.* Ocean Engineering, 188, pp. 106262.

[39] Mainon, P. (2004) *Inverse FEM I: load and response estimates from measurements.* In: Proceedings of the 2nd International Conference on Structural Engineering, Mechanics and Computation, 2004. Cape Town.

[40] Mainon, P. (2004) *Inverse FEM II: dynamic and non-linear problems.* In: Proceedings of the 2nd International Conference on Structural Engineering, Mechanics and Computation, 2004. Cape Town.

[41] Miller, E.J., Manalo, R. and Tessler, A. (2016) *Full-Field Reconstruction of Structural Deformations and Loads from Measured Strain Data on a Wing Using the Inverse Finite Element Method.* NASA/TM-2016-219407.

[42] Papa, U., Russo, S., Lamboglia, A., Del Core, G. and Iannuzzo, G. (2017) *Health structure monitoring for the design of an innovative UAS fixed wing through inverse finite element method (iFEM).* Aerospace Science and Technology, 69, pp. 439448.

[43] Quach, C., Vazquez, S., Tessler, A., Moore, J., Cooper, E. and Spangler, J. (2005) *Structural anomaly detection using fiber optic sensors and inverse finite element method.* In: Proceedings of the AIAA Guidance, Navigation, and Control Conference and Exhibit, 2005. San Francisco.

[44] Tessler, A. and Spangler, J.L. (2003) *A variational principal for reconstruction of elastic deformation of shear deformable plates and shells.* NASA/TM-2003-212445.

[45] Tessler, A. and Spangler, J.L. (2004) *Inverse FEM for full-field reconstruction of elastic deformations in shear deformable plates and shells.* In: Proceedings of the 2nd European Workshop on Structural Health Monitoring, 2004. Munich.

[46] Tessler, A., Spangler, J.L., Mattone, M., Gherlone, M. and Di Sciuva, M. (2011) *Real-time characterization of aerospace structures using onboard strain measurement technologies and inverse Finite element method.* In: Proceedings of the 8th International Workshop on Structural Health Monitoring, 2011. Stanford.

[47] Bruno, R., Toomarian, N. and Salama, M. (1994) *Shape estimation from incomplete measurements: a neural-net approach.* Smart Materials and Structures, 3(2), pp. 92-97.

[48] Mao, Z. and Todd, M. (2008) *Comparison of shape reconstruction strategies in a complex flexible structure.* Proc. SPIE 6932, Sensors and Smart Structures Technologies for Civil, Mechanical, and Aerospace Systems 2008. San Diego.

[49] Gherlone, M., Cerracchio, P. and Mattone, M. (2018) *Shape sensing methods: Review and experimental comparison on a wing-shaped plate.* Progress in Aerospace Sciences, 99, pp. 1426.

[50] Pak, C. (2016) *Wing Shape Sensing from Measured Strain.* AIAA Journal, 54(3), pp. 1068-1077.

[51] O' Callahan, J., Avitabile, P., and Riemer, R. (1988) *System Equivalent Reduction Expansion Process.* In: Proceedings of the 7th International Modal Analysis Conference, 1989. Las Vegas.

[52] Derkevorkian, A., Masri, S., Alvarenga, J., Boussalis, H., Bakalyar, J. and Richards, W. (2013) *Strain-Based Deformation Shape-Estimation Algorithm for Control and Monitoring Applications.* AIAA Journal, 51(9), pp. 2231-2240.

[53] Tessler, A. and Hughes, T.J. R. (1983) *An improved treatment of transverse shear in the mindlin-type four-node quadrilateral element.* Computer Methods in Applied Mechanics and Engineering, 39(3), pp. 311335.

[54] Cook, R.D. (1994) *Four-node flat shell element: Drilling degrees of freedom, membrane-bending coupling, warped geometry, and behavior.* Computers & Structures, 50(4), pp. 549555.

[55] Kefal, A. *Private communication.*